Modelling of the effect of the sheared poloidal flow on the electrostatic turbulence on the CASTOR tokamak *)

K. Dyabilin

Institute of High Energy Density, Moscow, Russian Federation

R. Klíma, I. Ďuran, J. Horáček, M. Hron, P. Pavlo, J. Stöckel, F. Žáček

Institute of Plasma Physics, Association EURATOM/IPP.CR, Prague, Czech Republic

Electrostatic drift turbulence of the edge plasma in the CASTOR tokamak is studied numerically by using the Hasegawa–Wakatani equations. The fluctuations of plasma density and potential as well as the corresponding fluctuation-induced particle flux are calculated for regimes with various plasma poloidal flows. Results of numerical simulations are in a reasonable agreement with experimental results.

1   Introduction

Turbulent convection connected with the drift-wave turbulence is widely believed to be responsible for the anomalous particle and energy losses in magnetized plasmas.

In the case of the edge plasma in tokamaks, the experimentally observed turbulent structures are of "flute-type". They form long filaments along the magnetic field lines mainly at the outboard side of the torus [1, 2]. They exist even in the case when the pressure gradient is well below the ideal ballooning instability threshold. This indicates that the dominant instability could be the pressure-driven interchange mode. Edge turbulence exhibits a strong poloidal asymmetry, what is observed on many tokamaks (see e.g. references in [3]). Moreover, according to experiments, the density and potential structures are similar to each other. Consequently, the possible mechanism of their coupling may be the collisional dissipation of the energy of particle motion along the magnetic field lines. The approach of Hasegawa and Wakatani [4, 5] is commonly accepted as a good approximation for modelling of such plasmas. This approximation was also used for modelling of the L–H transition and ELMs phenomena [6, 7]. Different regimes of the poloidal sheared flow were studied in [8].

In this paper, the edge turbulence is simulated by using the above mentioned model [4, 5], with the inclusion of sheared poloidal flows. The model is applied to the experimental conditions of the CASTOR tokamak, where the edge plasma can be externally polarized. For this purpose, an independently developed fluid model of polarized plasmas is used to calculate the equilibrium poloidal flows.

---

*) Presented at the 4th Europhysics Workshop "Role of Electric Fields in Plasma Confinement and Exhaust", Funchal, Madeira, Portugal, June 24–25, 2001

2   Description of the model

2.1   Basic equations

We start from the momentum and particle balance equations,

$$\rho \left(\frac{\partial \vec{v}}{\partial t} + (\vec{v} \, \nabla) \vec{v} \right) = -\nabla p + \vec{\jmath} \times \vec{B} - \nabla \cdot \hat{\pi} \; , \tag{1}$$

$$\frac{\partial n}{\partial t} + \nabla \cdot (n \vec{v}) = S \; , \tag{2}$$

where S is the particle source and the remaining notations are standard. The perpendicular flow velocity, $\vec{v}_\perp$, is expressed as:

$$\vec{v}_\perp = \frac{(\vec{B} \times \nabla \phi)}{B^2} + \frac{(\vec{B} \times \nabla p_{\mathrm{i}})}{enB^2} \; . \tag{3}$$

The electrostatic potential and density are assumed as:

$$n = n_0 + \tilde{n} \; ; \quad \phi = \phi_0 + \tilde{\phi} \; , \tag{4}$$

where the subscript "0" denotes poloidally averaged steady-state values and the tilde denotes the fluctuating parts. The toroidal magnetic field is approximated as:

$$B = \frac{B_0 R}{R + r \cos \theta} \; , \tag{5}$$

where θ is the poloidal angle, R and r are the major and the minor radii, respectively. The magnetic field at the plasma axis is denoted as B_0.

Applying the $(\nabla \times)_\parallel$ operator to the momentum balance equation (1), one obtains the equation for the plasma flow vorticity,

$$\omega = (\nabla \times \vec{v})_\parallel \approx \nabla_\perp^2 \phi / B \; . \tag{6}$$

The parallel momentum balance equations for electrons and the perpendicular pressure balance equation imply the values of the parallel and perpendicular currents:

$$j_\parallel = -env_\parallel = \frac{en_0 T_{\mathrm{e}}}{m_{\mathrm{e}} \nu_{\mathrm{ei}}} \nabla_\parallel \left(\frac{\tilde{n}}{n_0} - \frac{e\tilde{\phi}}{T_{\mathrm{e}}} \right) , \tag{7}$$

$$j_\perp = \frac{1}{B} \frac{\partial p}{\partial r} \; . \tag{8}$$

Finally, to reduce the dimensionality of the system, we use the single toroidal mode approximation:

$$\nabla_\parallel^2 \approx -\frac{1}{L_\parallel^2} \; , \tag{9}$$

where $L_\parallel$ is the characteristic parallel scale length of the density and potential structures, which will be specified below.

The resulting equations for the particle balance and the vorticity are written in the slab geometry. The coordinates x and y correspond to the radial and poloidal directions. The following quantities are normalized:

$$x, y \rightarrow x, y * \frac{1}{x_0} \; ; \quad t \rightarrow t * \frac{1}{\tau_0} \; ; \quad \phi \rightarrow \phi * \frac{e}{T_0} \; ; \quad T_{\mathrm{e}} \rightarrow T_{\mathrm{e}} * \frac{1}{T_0}, \qquad (10)$$

where x_0, T_0 are some characteristic values (see below), and $\tau_0 = \dfrac{x_0^2}{(T_0/eB)}$.

Normalized basic equations used for the numerical simulation then become:

$$\frac{\partial n}{\partial t} + (\nabla\phi \times \nabla n)_\parallel = \frac{\partial n_0}{\partial x}\frac{\partial \phi}{\partial y} - V_\theta \frac{\partial n}{\partial y} + \sigma_2 n_0 \left(\frac{\phi}{T_{\mathrm{e}}} - \frac{n}{n_0} \right) + D\nabla_\perp^2 n \qquad (11)$$

$$\frac{\partial \omega}{\partial t} + (\nabla\phi \times \nabla\omega)_\parallel = -G_{\mathrm{b}} \left(\frac{\cos\theta}{n_0}\frac{\partial n}{\partial y} + \frac{\sin\theta}{n_0}\frac{\partial n}{\partial x} + \frac{n}{n_0}\left(\frac{1}{T}\frac{\partial T}{\partial x} \right)\sin\theta \right)$$

$$+ \sigma_1 \left(\frac{\phi}{T_{\mathrm{e}}} - \frac{n}{n_0} \right) - V_\theta \frac{\partial \omega}{\partial y} + \frac{\partial^2 V_\theta}{\partial x^2}\frac{\partial \phi}{\partial y} + \mu \nabla_\perp^2 \omega \; , \quad (12)$$

$$\omega = \nabla_\perp^2 \phi \; , \qquad (13)$$

where

$$\sigma_1 = \frac{\omega_{\mathrm{ci}} v_{T_{\mathrm{e}}}^2}{\nu_{\mathrm{ei}} L_\parallel^2}\tau_0^2 \; ; \quad \sigma_2 = \frac{v_{T_{\mathrm{e}}}^2}{\nu_{\mathrm{ei}} L_\parallel^2}\tau_0 \; ; \quad G_{\mathrm{b}} = \frac{c_{\mathrm{s}}^2}{x_0 R}\tau_0^2 \; ; \quad T = T_{\mathrm{e}} + T_{\mathrm{i}} \; . \qquad (14)$$

In the above equations, V_θ is the steady state poloidal flow velocity. The coefficients σ_1 and σ_2 (known as the adiabaticity parameters) determine the degree of Boltzmann coupling between the density and potential fluctuations. The symbols D and μ denote the coefficients of diffusion and kinematic viscosity, normalized to the value $0.1 \ \mathrm{m^2 s^{-1}}$.

2.2   Geometry and input parameters

Calculations are performed for the geometry of the CASTOR tokamak, with the major radius $R = 0.4$ m and the minor radius of the vacuum vessel $r_{\mathrm{ch}} = 0.1$ m. The confinement region is restricted by the poloidal limiter with the radius $a = 0.085$ m. The toroidal magnetic field is typically $B = 1$ T and the plasma current is in the range of $I_{\mathrm{p}} = (10\text{--}15)$ kA. This yields the safety factor at the separatrix $q(r = a) = 8\text{--}10$. At such discharges, the line averaged density is $\bar{n} = 10^{19} \ \mathrm{m^{-3}}$, the central electron and ion temperatures are $T_{\mathrm{e0}} = (150\text{--}200)$ eV and $T_{\mathrm{i0}} = (50\text{--}80)$ eV, respectively.

According to these typical parameters, we choose in Eqs. (10): $x_0 = 5$ mm, $T_0 = 25$ eV. For the magnetic field $B = 1$ T, we get the characteristic time $\tau_0 = 1 \ \mu$s.

The system of equations is solved on a rectangular grid of (100×1256) points corresponding to the (*radial* × *poloidal*) directions. The grid is uniform in both
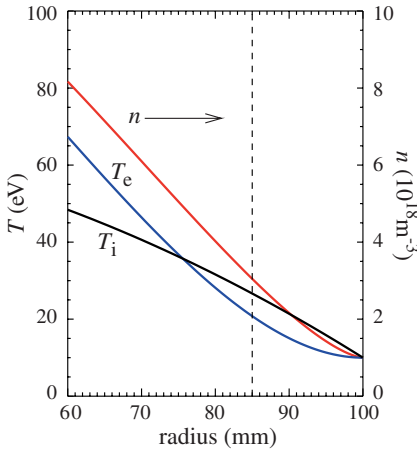
Fig. 1. Radial profiles of plasma density and electron/ion temperatures assumed in simulations.
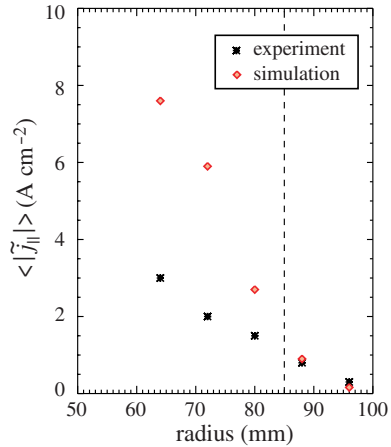
Fig. 2. Radial profile of the parallel current fluctuations: simulation (diamonds) and experiment (stars).

directions. The radial coordinates extend from $r = 0.06$ m up to $r = 0.1$ m and the poloidal angles are $(0–2)\pi$. The profiles of plasma density and electron/ion temperatures, chosen as an input for modelling, are shown in Fig. 1. The boundary conditions of all variables are set zero for both radii limiting the region considered. In the poloidal direction, the condition of periodicity must be fulfilled. The initial conditions are chosen as randomly distributed perturbations of density and potential at the relative level of 10^{-6}–10^{-7}.

2.3 Parallel scale length of perturbations

The parallel scale length $L_\parallel$ in the scrape-off layer is obviously given by the circumference of the torus

$$L_\parallel = 2\pi R ; \quad r \geq a .\tag{15}$$

In the confinement region $(r < a)$, the parallel gradient can be expressed as $\nabla_\parallel = \frac{1}{R}\partial_\varphi + \frac{1}{qR}\partial_\theta \approx \frac{1}{qR}\partial_\theta$ and, consequently,

$$L_\parallel = 2\pi R q(r) ; \quad r < a .\tag{16}$$

The safety factor $q(r)$ is calculated from the ohmic current profile, which is given by the input T_e-profile on assumption of the Spitzer resistivity.

The validity of the above estimate of $L_\parallel$ has been verified "a posteriori" by comparison of the parallel current density fluctuations experimentally measured on CASTOR by means of a small Rogowski coil [9] with those deduced from the simulations. The computed and experimental profiles of root mean square (*rms*) values of $j_\parallel$ fluctuations are compared in Fig. 2. In the scrape-off-layer (SOL), the coincidence is surprisingly good. In the confinement region, the simulation values

1110

are higher than the experimental ones. This may be due to a limited accuracy caused by the strong dependence of $j_\parallel$ on the electron temperature. Thus, on the whole, the above estimate of $L_\parallel$ appears to be acceptable.

2.4 Poloidal flow velocity

The radial electric field in tokamaks as well as plasma poloidal flow is governed by the ion poloidal force balance. The corresponding equation averaged over the magnetic surfaces is:

$$(1+2q^2)\rho\frac{\mathrm{d}V_\theta}{\mathrm{d}t} = J_r B_0 - F_{\text{visc}} - F_{\text{i0}} + (1+2q^2)\nabla\cdot(\eta\nabla V_\theta) \quad , \qquad (17)$$

where $\rho = M_{\text{i}}n$ is the mass density, $V_\theta = -E/B_0 + V_{\text{d}}$ is the poloidal velocity due to both the $\mathbf{E}\times\mathbf{B}$ and the diamagnetic drifts (with the velocity $V_{\text{d}} = \nabla p_{\text{i}}/(eB_0 n)$). The contribution from the toroidal velocity component has been neglected. Further, $\mathrm{d}/\mathrm{d}t = (\partial/\partial t + V_r\nabla_\perp)$, where V_r is the radial velocity defined by the radial ion flux as $nV_r = \Gamma_{\text{i}}$. The factor $(1+2q^2)$ appears due to flux surface averaging [10]. The poloidal rotation is driven by the radial current J_r. The damping mechanisms included into the balance equation are the parallel ion viscosity (F_{visc}), the friction force due to the ion-neutral collisions (F_{i0}) and the damping due to the transverse viscosity. More details are given in [11].

In the limiter shadow, parallel electric currents lead to the plasma radial polarization and, consequently, to its poloidal rotation. Steady-state radial profiles of the plasma potential and poloidal velocity computed by this model are presented in Fig. 3a. The radial profile of the plasma potential is consistent with that measured
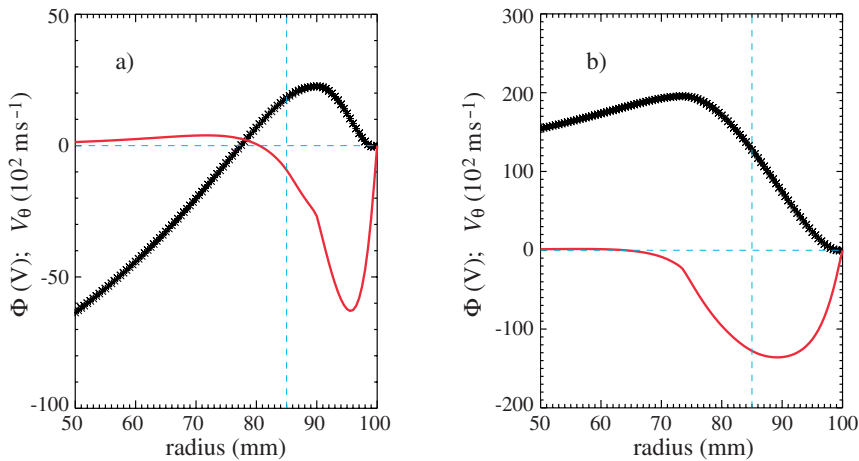

Fig. 3. Radial profiles of the plasma potential (thick line) and the poloidal flow velocity (thin line) a) in the case with the limiter-induced flow, and b) with biasing (electrode position $r = 70$ mm; biasing voltage $U_{\text{b}} = +200$ V.

by Langmuir probes at the CASTOR edge [12]. Also, the poloidal flow velocities measured by the rotating Mach probe technique are within 0.1–0.2 of the ion sound velocity [13, 14], in agreement with the computed V_θ. Figure 3b shows the same profiles in the case of biasing (with the electrode positioned at $r = 70$ mm and biased up to $U_b = +200$ V, see Subsect. 3.2. In this case, the flow velocity increases in the whole region between the electrode and the wall.

3   Results of modelling

Numerical solution of Eqs. (11)–(13) yields the spatial and temporal distribution of the potential and density fluctuations at the plasma edge of the CASTOR toka-mak. Then, the radial profiles of *rms* values of fluctuating quantities, their power spectra and the spatial correlation lengths are derived. Finally, the fluctuation-induced particle flux is computed.

3.1   Turbulence at $V_\theta = 0$

The snap-shots of the density and potential structures are shown in Fig. 4. It is seen that they are of a similar character, which is obviously because of their strong coupling. Such saturated level of turbulence is developed in a few hundreds of microseconds (for the CASTOR case).

In accordance with the unfavorable curvature of the magnetic field lines, the turbulent structures appear at first in the low field side region of the torus, $-\pi/2 < \theta < \pi/2$. Then, they are redistributed poloidally, reaching a dynamic equilibrium. However, the poloidal asymmetry remains not only in the "in-out" direction, but it develops also in the "top-bottom" direction. In what follows, we will present results concerning the regime of saturated turbulence.
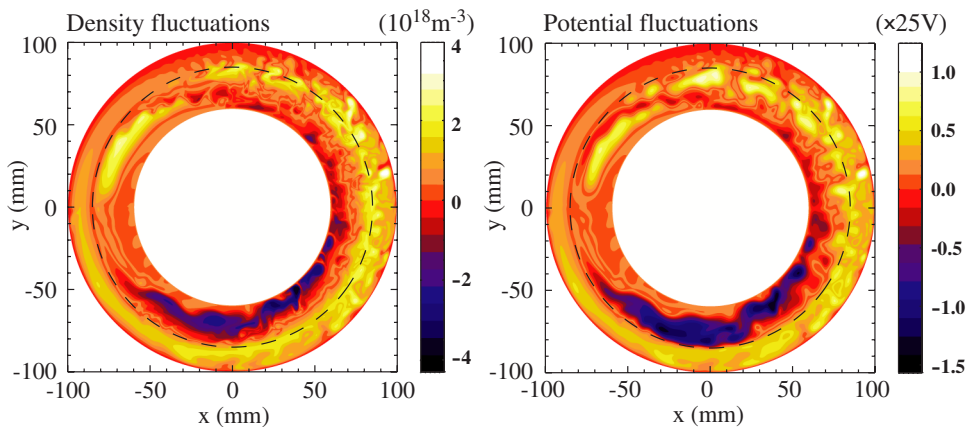

Fig. 4.   Snap-shots of turbulent structures. Left: plasma density, the scales in 10^{18}m^{-3}. Right: plasma potential normalised to 25 V.

Detailed pictures of the potential structures at the top of the torus are given in Fig. 5a–c. The individual panels represent the situation in three consequent moments. It is seen that the characteristic poloidal and radial dimensions of potential structures are about (5–10) mm. Typical characteristic life time of the structures is of the order of 10 μs. The poloidal and radial correlation lengths, derived from the spatial-temporal correlation analysis of the computed data are in the same range. This is in agreement with pictures, obtained in experiments performed on the CASTOR tokamak using a 2-D matrix of Langmuir probes [15], see Fig. 5d. The figure is in scale with a–c. The matrix of probes is positioned at the top of the torus.

Spectral analysis of the fluctuation data computed at the separatrix ($r =$ 85 mm) are presented in Fig. 6a. Three frequency bands, with the power spec-
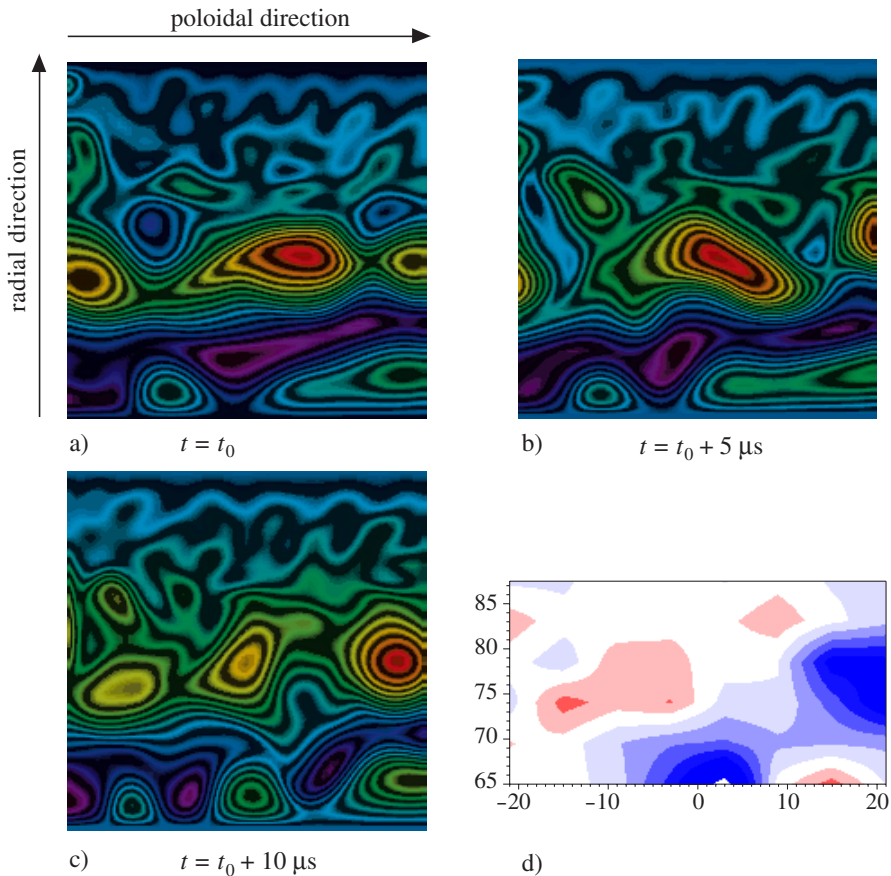

Fig. 5. a-c): Three snap-shots of potential structures at the top of the torus. Each panel depicts the area of 40 mm × 40 mm. d): Potential structures measured by a 2-D matrix of Langmuir probes (in scale with a–c).
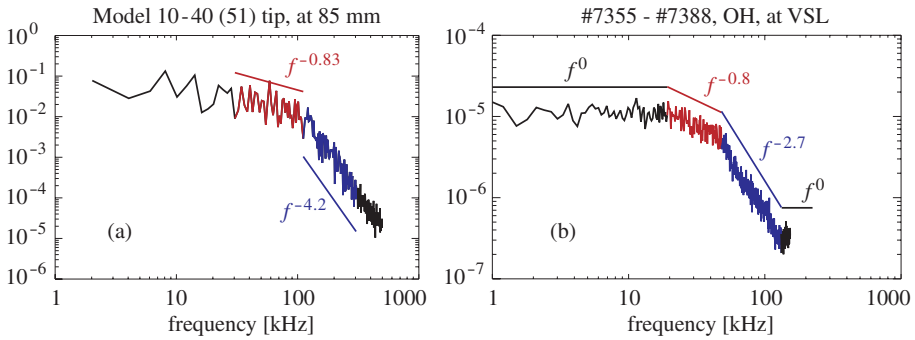
Fig. 6. Power spectra of potential fluctuations at the top of the torus and $r = 85$ mm (separatrix): a) derived from simulation; b) experimentally measured by a probe.
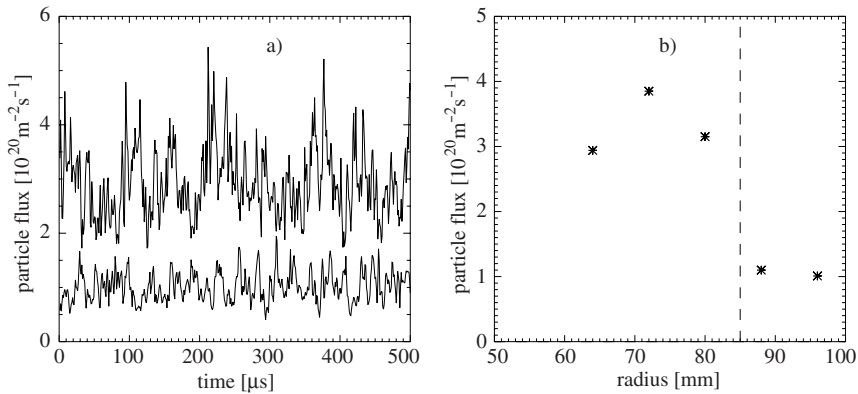

Fig. 7. a) Temporal evolution of the poloidally averaged particle flux. Radial positions $r = 64$ mm (upper trace) and $r = 96$ mm (lower trace). b) Radial profile of the poloidally averaged particle flux.

trum density decaying as $f^{-\alpha}$ are apparent, the corresponding exponents being $\alpha \approx 0$, 0.83, and 4.2. Apart from the very low power spectra densities, the above mentioned exponents are close to the experimentally measured values, cf. Fig. 6b.

The fluctuation-induced flux can be calculated from the simulation results as

$$nv_r = [n_0(x) + \tilde{n}]\frac{(\vec{B} \times \nabla\tilde{\phi})_r}{B^2} \ . \tag{18}$$

Figure 7a shows the temporal evolution of the poloidally averaged flux

$$\langle nv_r \rangle = \frac{1}{2\pi} \int_0^{2\pi} nv_r(\theta)\left(1 + \frac{r}{R}\cos\theta\right) \mathrm{d}\theta \tag{19}$$

for two radial positions. It is seen that the averaged flux density is always positive (outward). Radial profile of the flux, averaged over time and poloidal angle is shown

1114

in Fig. 7b. In the vicinity of the separatrix, the flux decreases nearly three times as compared with that in the confinement region. It should be noted that the global particle confinement time on the CASTOR tokamak is (1–2) ms. This implies the global particle flux across the separatrix in the range of $(2\text{--}4) \times 10^{20}$ m^{-2}s^{-1}. As seen from Fig. 7b, the numerical simulation yields values close to these numbers.

3.2 Turbulence at $V_\theta \neq 0$

As already mentioned, limiter-induced parallel electric currents lead to plasma radial polarization and, consequently, to its poloidal rotation (cf. Fig. 3). The rotation can be also induced or enhanced by means of external plasma polarization, e.g. by a biasing electrode [16]. This was successfully demonstrated also on the CASTOR tokamak [12]. Here, the carbon mushroom electrode can be inserted into the plasma column from the top of the torus, $\approx 80^\circ$ toroidally away from the ion side of the limiter. Its poloidal extension is ≈ 50 mm.

The poloidal flow strongly affects the plasma turbulence. Fig. 8a shows the temporal evolution of the fluctuation-induced flux in the confinement region (at $r = 80$ mm) with limiter-induced current and with the biasing (switched on at $t = 100\,\mu$s). The characteristic transition time of the flux change is less than $100\,\mu$s. Fig. 8b gives the radial profile of the average fluctuation-induced flux without and with the biasing. The flux is significantly reduced owing to the limiter-induced flow, and still more so with the biasing (cf. Figures 7 vs. 8).

The influence of the poloidal flows on the spatial and temporal behaviour of the fluctuation induced flux can be seen in more detail from Fig. 9. Here, the evolution of the radial profiles of the particle flux at the top of the torus is shown. Figure 9a corresponds to the regime, when the flow is absent. Figure 9b is the case of limiter induced flow and biasing (switched on at $t = 100\,\mu$s). In the regions where the flow
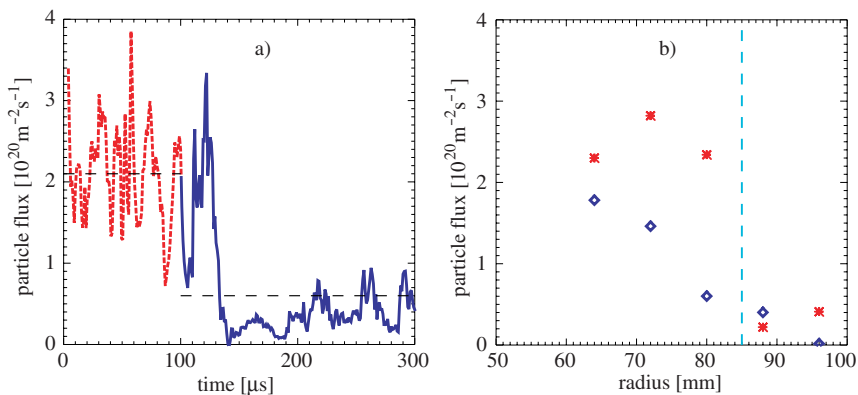

Fig. 8. a) Temporal evolution of the poloidally averaged flux with limiter-induced flows and biasing. Radial positions $r = 80$ mm, biasing is switched on at $100\,\mu$s. b) Radial profile of averaged fluctuation induced flux with (diamonds) and without (stars) biasing.
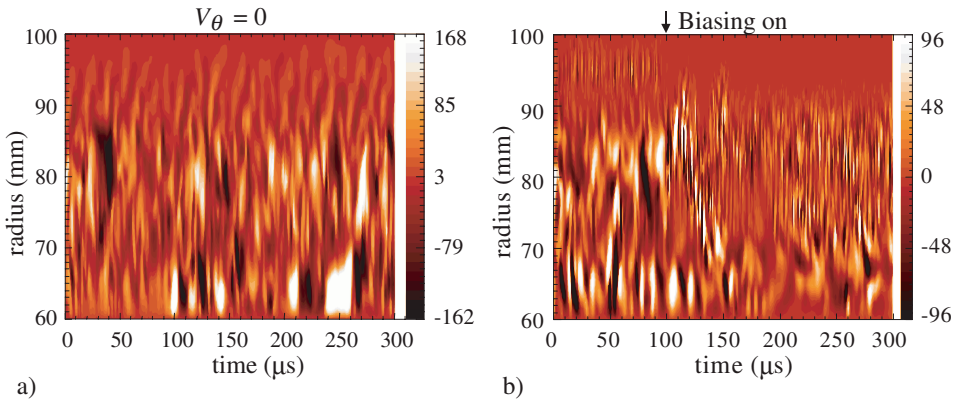
Fig. 9. Temporal evolution of the radial particle flux deduced from simulation at the top of the torus: a) in the case without a steady-state poloidal flow, b) with the plasma poloidal flow induced by the limiter and biasing (switched on at 100 ms). The scale is in $10^{20}\,\mathrm{m}^{-2}\mathrm{s}^{-1}$.

velocity shear is strong enough (cf. Fig. 3), the level of fluctuations is reduced. Note that in the low-shear region ($r \approx 96\,\mathrm{mm}$), the characteristic time of the fluctuations decreases. These features become even more pronounced in case of plasma external polarization with a broader region of high flow velocity.

4   Conclusions

The 2-D system of the Hasegawa and Wakatani equations was solved numerically in the region of the limiter shadow and its vicinity. The input parameters were chosen according to the tokamak CASTOR conditions. Various regimes including externally polarized plasma were studied. In general, results of modelling exhibit a good agreement with the experimental data:

- the characteristic dimensions and time scales of the density and potential structures are close to the measured ones;
- the value of the fluctuation induced particle flux is comparable with that measured in the experiment;
- sheared plasma poloidal flows strongly affect the turbulent structures; the resulting particle flux reduces remarkably in agreement with experimental data.

However, some features, e.g. the shape of the frequency spectra (for $f > 70\,\mathrm{kHz}$), do not agree with the experiment.

Finally, we remark that the estimate of the characteristic parallel scale length as well as the reduction of the system of equations to the 2-D case (see e.g. [17]) require further studies.

References

[1] H. Niedermeyer et al.: in *Proc. 18th Europen Conference on Controlled Fusion and Plasma Physics*, Berlin 1991, IAEA, Vienna, 1991, Vol. 1, p. 301.

[2] E. Endler et al.: in *Proc. 20th International Conference on Controlled Fusion and Plasma Physics*, Lisboa 1993, IAEA, Vienna, 1993, Vol. 2, p. 583.

[3] X. Garbet, C. Fenzi, H. Capes, P. Devynck, and G. Antar: Phys. Plasmas **6** (1999) 3955.

[4] A. Hasegawa and M. Wakatani: Phys. Rev. Lett. **50** (1985) 682.

[5] M. Wakatani and A. Hasegawa: Phys. Fluids **27** (1984) 611.

[6] S. Camargo, D. Biscamp, B. Scott: Phys. Plasmas **2** (1995) 1.

[7] O. Pogutse, W. Kernel, V. Gribkov, S. Bazdenkov, M. Osipenko: Plasma Phys. Control. Fusion **36** (1994) 1963.

[8] R.V. Shurygin: Fizika Plazmi **25** (1999) 739 (in Russian).

[9] I. Duran et al.: in *Proc. 26th EPS Conf. Contr. Fusion Plasma Phys.*, Maastricht 1999, EPS, Mulhouse, ECA **23J** (1999) 714.

[10] V. Rozhansky, M. Tendler: *Reviews of Plasma Physics* (Consultants Bureau: N.Y.) **19** (1996) 147.

[11] K. Dyabilin et al.: *Modelling of electrostatic turbulence at the edge of the CASTOR tokamak*, Research Report IPPCZ-366, December 2000 (available at IPP AS CR, Prague).

[12] J. Stockel et al.: *Proc. 26th EPS Conf. Contr. Fusion Plasma Phys.*, Maastricht 1999, EPS, Mulhouse, ECA **23J** (1999) 1589.

[13] J.P. Gunn: Bull. Am. Phys. Soc. **45** (2000) 185.

[14] K. Dyabilin et al.: *Proc. 27th EPS Conf. Contr. Fusion Plasma Phys.*, Budapest 2000, EPS, Mulhouse, ECA **24B** (2000) 1653.

[15] J. Stöckel et al.: *ibid.*, p.1032.

[16] R.R. Weynants and G. Van Oost: Plasma Phys. Contr. Fusion **35** (1993) B177.

[17] P. Beyer, Y. Sazarin, X. Garbet, P. Ghendrih, and S. Benkadda: Plasma Phys. Contr. Fusion **41** (1999) A757.